Equivalent-Circuit Models for Grid-Forming Inverters under Unbalanced Steady-State Operating Conditions

Preprint

Nathan Baeckeland,[1] Gab-Su Seo,[1] Alejandro Dominguez-Garcia,[2] Deepak Ramasubramanian,[3] Dominic Gross,[4] and Sairaj Dhople[5]

1 National Renewable Energy Laboratory
2 University of Illinois
3 Electric Power Research Institute
4 University of Wisconsin-Madison
5 University of Minnesota

To be presented at the 2025 Hawaii International Conference on System Sciences (HICSS)
Waikoloa Village, Hawaii
January 7–10, 2025

NREL is a national laboratory of the U.S. Department of Energy
Office of Energy Efficiency & Renewable Energy
Operated by the Alliance for Sustainable Energy, LLC

This report is available at no cost from the National Renewable Energy Laboratory (NREL) at www.nrel.gov/publications.

Contract No. DE-AC36-08GO28308

Conference Paper
NREL/CP-5D00-90519
November 2024

Equivalent-Circuit Models for Grid-Forming Inverters under Unbalanced Steady-State Operating Conditions

Preprint

Nathan Baeckeland,[1] Gab-Su Seo,[1] Alejandro Dominguez-Garcia,[2] Deepak Ramasubramanian,[3] Dominic Gross,[4] and Sairaj Dhople[5]

1 National Renewable Energy Laboratory
2 University of Illinois
3 Electric Power Research Institute
4 University of Wisconsin-Madison
5 University of Minnesota

Suggested Citation
Baeckeland, Nathan, Gab-Su Seo, Alejandro Dominguez-Garcia, Deepak Ramasubramanian, Dominic Gross, and Sairaj Dhople. 2024. *Equivalent-Circuit Models for Grid-Forming Inverters under Unbalanced Steady-State Operating Conditions: Preprint*. Golden, CO: National Renewable Energy Laboratory. NREL/CP-5D00-90519. https://www.nrel.gov/docs/fy25osti/90519.pdf.

NREL is a national laboratory of the U.S. Department of Energy
Office of Energy Efficiency & Renewable Energy
Operated by the Alliance for Sustainable Energy, LLC

This report is available at no cost from the National Renewable Energy Laboratory (NREL) at www.nrel.gov/publications.

Contract No. DE-AC36-08GO28308

Conference Paper
NREL/CP-5D00-90519
November 2024

National Renewable Energy Laboratory
15013 Denver West Parkway
Golden, CO 80401
303-275-3000 • www.nrel.gov

NOTICE

This work was authored in part by the National Renewable Energy Laboratory, operated by Alliance for Sustainable Energy, LLC, for the U.S. Department of Energy (DOE) under Contract No. DE-AC36-08GO28308. This work was supported by the Laboratory Directed Research and Development (LDRD) Program at NREL and the U.S. Department of Energy Office of Energy Efficiency and Renewable Energy under the Solar Energy Technologies Office Award Number 38637. This research was also supported by the Grid Modernization Initiative of DOE as part of its Grid Modernization Laboratory Consortium, a strategic partnership between DOE and the national laboratories to bring together leading experts, technologies, and resources to collaborate on the goal of modernizing the nation's grid. The views expressed herein do not necessarily represent the views of the DOE or the U.S. Government.

Equivalent-circuit Models for Grid-forming Inverters under Unbalanced Steady-state Operating Conditions

Nathan Baeckeland
Power Systems Engineering Center,
National Renewable Energy Laboratory
nathan.baeckeland@nrel.gov

Alejandro Domínguez-García
University of Illinois
Urbana-Champaign
aledan@illinois.edu

Dominic Gross
University of Wisconsin-Madison
dominic.gross@wisc.edu

Sairaj Dhople
University of Minnesota
sdhople@umn.edu

Gab-Su Seo
Power Systems Engineering Center,
National Renewable Energy Laboratory
gabsu.seo@nrel.gov

Deepak Ramasubramanian
Electric Power Research Institute
dramasubramanian@epri.com

Abstract

Positive- and negative-sequence equivalent-circuit models are put forth to capture the operation of grid-forming (GFM) inverters in unbalanced steady-state operating conditions acknowledging the impact of current limiting. The particular control architecture examined adopts droop control (for primary control), nested inner-current and outer-voltage control (in the stationary reference frame), and it is adaptable to two different types of current limiting (current-reference saturation and virtual-impedance limiting). We anticipate the proposed models to be of interest in modeling, analysis, and simulation of GFM inverters in unbalanced settings that may arise, e.g., in the face of faults. Validation of the equivalent-circuit models is pursued via comparison with full-order electromagnetic-transient (EMT) simulations for representative balanced and unbalanced faults.

Keywords: Equivalent-circuit models, fault analysis, grid-forming inverters, power systems, unbalanced faults.

1. Introduction

Grid-forming (GFM) controls for inverter-based resources (IBRs) continue to garner sustained interest across academia and industry worldwide. A variety of issues currently dominate research and development agendas, and of these, modeling, analysis, and control of GFM IBRs during balanced and unbalanced faults on the grid are particularly unsettled aspects [1, 2]. Driving convergent advances on these topics requires synergizing (analytical and computational) efforts across power electronics and power systems domains. Taking a step in this direction, this paper puts forth a framework to obtain equivalent-circuit models for GFM IBRs that capture their steady-state operation during unbalanced steady-state operating conditions that may be brought on, e.g., by faults on the grid.

We illustrate the derivation of the equivalent-circuit model for a stationary-frame control architecture with droop control adopted for primary control and proportional-resonant controllers for inner-current and outer-voltage control [3]. Within this architecture, two different types of current limiting—current-reference saturation (SatLim) [4, 5, 6] and threshold virtual impedance (VI-Lim) [7, 3, 8]—are examined. This is one of several architectures [4, 5, 8] that have been proposed for unbalanced operation in the literature (our review of related efforts appears shortly). Nonetheless, this specific instantiation provides a means to highlight key ideas. The derivation of the equivalent circuit model is presented in a systematic procedure that can be applied to other control architectures (i.e., other primary controls, reference frames for control, and types of current limiters). We leverage a combination of reference-frame transformations, the notion of dynamic phasors, and theory of symmetrical components to arrive at positive- and negative-sequence equivalent circuits for the GFM IBRs. Notably, these equivalent circuits capture the impact of current limiting (SatLim and VI-Lim) and are applicable to unbalanced settings.

With regard to related prior art, we point to a variety of recent efforts in synthesizing controllers for GFM IBRs that are resilient to unbalanced settings and faults, e.g., in [3, 4, 5, 8, 9, 10, 11, 12, 13, 14, 15]. While broad consensus on universal attributes has not been achieved, we see several recurring elements that are represented in the control architecture we examine. For instance, current limiting via some form of reference saturation [4, 5] or virtual impedance [3,

8] appears quite common. Similarly, nested voltage and current control loops that are commonly deployed in standard (i.e., balanced) operation carry over [3, 5]. These observations suggest that the approach adopted for deriving the equivalent circuits in this effort for our particular control architecture ought to translate broadly. We also point to several efforts in power-flow analysis of GFM IBRs in balanced [16, 17] and unbalanced settings [10, 18, 19] that our models would find immediate applicability in. Finally, equivalent-circuit models for IBRs have been put forth for a variety of IBR control architectures, including for GFM IBRs [6, 19, 20, 21, 22, 23]. Compared to these prior works, our models are derived in a more detailed and systematic way from the originating differential equations describing the dynamics of control- and physical-layer subsystems. This allows extrapolation to other GFM control architectures. Crucially, our models illustrate how various current-limiter designs can be featured in the equivalent circuit, and in particular, our proposed equivalent-circuit models for both current limiting strategies offer a similar underlying structure.

We anticipate these models being valuable to practicing engineers and academic researchers for a variety of applications. An immediate one is the ability to compute steady-state inverter output signals during normal and faulty operation which can aid power system protection studies and the assessment of relay functions such as fault-loop impedance computations. Furthermore, the models can be incorporated into power flow studies (involving other assets including grid-following inverters and synchronous machines). Finally, it is possible to derive power-angle curves of GFM inverters with various current limiters and primary controllers as well as compute stable and unstable equilibrium operating points. These are essential ingredients in large-signal stability analysis.

The remainder of this paper is organized as follows. In Section 2, we outline the control architecture for the GFM IBR built out with proportional resonant controllers in the stationary reference frame. Section 3 outlines the development of positive- and negative-sequence equivalent circuits that describe the steady-state operation of the GFM IBR. Simulation results to validate the equivalent circuit are in Section 4. Finally, we conclude with a few directions for future work in Section 5.

Notation

We represent signals in the synchronous reference frame as $X_{\mathrm{dq}} = [X_{\mathrm{d}},\, X_{\mathrm{q}}]^{\top}$, in the stationary reference frame as $x_{\alpha\beta} = [x_{\alpha}(t),\, x_{\beta}(t)]^{\top}$, and in the natural reference frame as $x_{\mathrm{abc}} = [x_{\mathrm{a}}(t),\, x_{\mathrm{b}}(t),\, x_{\mathrm{c}}(t)]^{\top}$. Counter-clockwise rotation of a vector by angle θ in the Euclidean space is captured by

$$\Gamma(\theta) = \begin{bmatrix} \cos\theta & -\sin\theta \\ \sin\theta & \cos\theta \end{bmatrix}.$$

In the time domain, we denote positive and negative sequence signals as x^{+} and x^{-}, respectively. In the dq frame, we denote positive and negative sequence signals as X^{+} and X^{-}, respectively. Further, to conserve space, we use the notation $x^{\pm}$, $X^{\pm}$ to denote variables in equations that apply to positive- and negative-sequence signals. A balanced set of signals, i.e., signals with the same amplitude and $\frac{2\pi}{3}$ phase shifted in the natural reference frame, can be represented as a dynamic complex phasor [24, 25]. We denote complex phasors by $\underline{X}\mathrm{e}^{\jmath\omega t}$, where the underscore denotes a complex scalar, $\jmath$ denotes the imaginary unit, and ω denotes the angular speed of the dynamic phasor.

2. GFM Control Architecture

Figure 1 illustrates the three-phase three-wire GFM control architecture that serves as the baseline for this study. For better handling during unbalanced conditions, the control system is built in the stationary reference frame. The entire stationary-frame GFM control structure in Fig. 1, along with tuning techniques and current-limiter design is outlined in detail in [3]. For clarity, we briefly introduce the GFM controls. The inverter-side current, $i^{\mathrm{i}}_{\mathrm{abc}}$, the capacitance voltage, e_{abc}, and the grid-side current, $i^{\mathrm{g}}_{\mathrm{abc}}$, of the LCL-filter are measured and transformed into the stationary reference frame using Clark's transformation. Based on the output measurements, and the power setpoints, $P^{\star}$, $Q^{\star}$, the primary controller generates the reference voltage and frequency/angle. From there, the reference voltage, $e^{\star}_{\alpha\beta}$, feeds into the voltage controller, which leverages a proportional-resonant controller. The output of the voltage controller drives the current controller, which in turn, outputs the reference signals for the switches in the H-bridge.

To curtail the output current during disturbances in the grid, we consider two well-known current-limiting concepts: the current-reference saturation limiter or magnitude limiter (SatLim), illustrated in yellow in Fig. 1, and the threshold virtual impedance limiter (VI-Lim), illustrated in blue in Fig. 1. Initiating switch $\mathcal{S}_1$ and $\mathcal{S}_2$ in Fig. 1 activates the VI-Lim and deactivates the SatLim. Both of these limiters are designed in the $\alpha\beta$-frame and limit the output current such that none of the phase currents exceeds the threshold, even

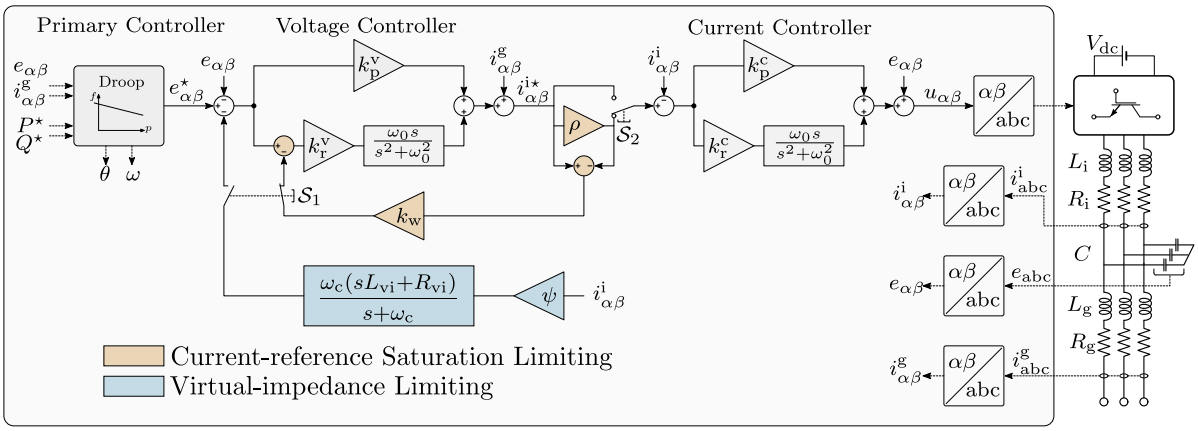

Figure 1. GFM control architecture with primary controller (droop control), inner-current, and outer-voltage control loops. Current limiting is implemented via either saturation limiting (SatLim) or virtual-impedance limiting (VI-Lim); initiating switch $\mathcal{S}_1$ and $\mathcal{S}_2$ activates the VI-Lim and deactivates the SatLim.

during unbalanced operating conditions. Dynamics of the different subsystems are described next.

2.1. Output LCL Filter

The dynamics of the LCL filter are captured by:

$$L_{\mathrm{g}}\tfrac{\mathrm{d}}{\mathrm{d}t}i^{\mathrm{g}}_{\mathrm{abc}} = e_{\mathrm{abc}} - v_{\mathrm{abc}} - R_{\mathrm{g}}i^{\mathrm{g}}_{\mathrm{abc}}, \tag{1a}$$

$$C\tfrac{\mathrm{d}}{\mathrm{d}t}e_{\mathrm{abc}} = i^{\mathrm{i}}_{\mathrm{abc}} - i^{\mathrm{g}}_{\mathrm{abc}}, \tag{1b}$$

$$L_{\mathrm{i}}\tfrac{\mathrm{d}}{\mathrm{d}t}i^{\mathrm{i}}_{\mathrm{abc}} = u_{\mathrm{abc}} - e_{\mathrm{abc}} - R_{\mathrm{i}}i^{\mathrm{i}}_{\mathrm{abc}}, \tag{1c}$$

where L_{g} and R_{g} denote the grid-side filter inductance and resistance, respectively, C denotes the filter capacitance, and L_{i} and R_{i} denote the inverter-side filter inductance and resistance, respectively.

2.2. Current Controller

Below, we discuss the dynamics of the current controller with saturation limiting and virtual impedance limiting separately.

SatLim. The dynamics of the current controller with SatLim are given by

$$\tfrac{1}{\omega_0^2}\tfrac{\mathrm{d}^2}{\mathrm{d}t^2}\gamma^{\mathrm{c}}_{\alpha\beta} = k^{\mathrm{c}}_{\mathrm{r}}(\rho i^{\mathrm{i}\star}_{\alpha\beta} - i^{\mathrm{i}}_{\alpha\beta}) - \gamma^{\mathrm{c}}_{\alpha\beta}, \tag{2a}$$

where $\gamma^{\mathrm{c}}_{\alpha\beta}$ denotes an internal state variable of the current controller, $k^{\mathrm{c}}_{\mathrm{r}}$ denotes the resonant gain, and $i^{\mathrm{i}\star}_{\alpha\beta}$ denotes the reference signal for the inverter-side filter current (for details on how this is determined, see subsequent discussion on the voltage controller in Section 2.3). The reference feeding into the current controller is scaled by the saturation gain, ρ, which is defined as:

$$\rho = \min\left(1,\ \tfrac{I_{\max}}{\|I^{\mathrm{i}\star}_{\mathrm{abc}}\|_\infty}\right), \tag{2b}$$

where $\|I^{\mathrm{i}\star}_{\mathrm{abc}}\|_\infty$ denotes the infinity norm of the reference currents generated by the voltage controller in the natural reference frame. This way, the terminal output currents are scaled relative to the highest phase current to guarantee correct current limiting during unbalanced conditions. This approach to reference saturation is one of several suggested in the literature. While specific implementations indeed vary, the underlying principle of scaling the current reference to curtail the output is a common theme. The current controller generates the modulation signal for the inverter switched terminals, $u_{\alpha\beta}$:

$$u_{\alpha\beta} = \tfrac{1}{\omega_0}\tfrac{\mathrm{d}}{\mathrm{d}t}\gamma^{\mathrm{c}}_{\alpha\beta} + e_{\alpha\beta} + k^{\mathrm{c}}_{\mathrm{p}}(\rho i^{\mathrm{i}\star}_{\alpha\beta} - i^{\mathrm{i}}_{\alpha\beta}), \tag{2c}$$

where $k^{\mathrm{c}}_{\mathrm{p}}$ denotes the proportional gain. (Since we use averaged-value models, $u_{\alpha\beta}$ equals the reference signal generated by the current controller.)

VI-Lim. When leveraging the VI-Lim, the current controller dynamics are given by

$$\tfrac{1}{\omega_0^2}\tfrac{\mathrm{d}^2}{\mathrm{d}t^2}\gamma^{\mathrm{c}}_{\alpha\beta} = k^{\mathrm{c}}_{\mathrm{r}}(i^{\mathrm{i}\star}_{\alpha\beta} - i^{\mathrm{i}}_{\alpha\beta}) - \gamma^{\mathrm{c}}_{\alpha\beta}, \tag{3a}$$

and the reference voltage is determined as

$$u_{\alpha\beta} = \tfrac{1}{\omega_0}\tfrac{\mathrm{d}}{\mathrm{d}t}\gamma^{\mathrm{c}}_{\alpha\beta} + e_{\alpha\beta} + k^{\mathrm{c}}_{\mathrm{p}}(i^{\mathrm{i}\star}_{\alpha\beta} - i^{\mathrm{i}}_{\alpha\beta}). \tag{3b}$$

The lack of scaling of the current reference (by ρ) is the only distinguishing attribute compared to the dynamics of the SatLim discussed previously.

2.3. Voltage Controller

SatLim. The dynamics of the voltage controller when leveraging the SatLim are

$$\tfrac{1}{\omega_0^2}\tfrac{\mathrm{d}^2}{\mathrm{d}t^2}\gamma^{\mathrm{v}}_{\alpha\beta} = k^{\mathrm{v}}_{\mathrm{r}}(e^{\star}_{\alpha\beta} - e_{\alpha\beta} - k_{\mathrm{w}}(1-\rho)i^{\mathrm{i}\star}_{\alpha\beta}) - \gamma^{\mathrm{v}}_{\alpha\beta}, \tag{4a}$$

where $\gamma^{\mathrm{v}}_{\alpha\beta}$ denotes an internal state variable of the voltage controller, $k^{\mathrm{v}}_{\mathrm{r}}$ denotes the resonant gain, k_{w} is the gain of the anti-windup controller, and $e^{\star}_{\alpha\beta}$ is the voltage reference from the primary controller (discussed in detail subsequently in Section 2.4). The reference for the current controller, $i^{\mathrm{i}\star}_{\alpha\beta}$, is determined by the voltage controller as

$$i^{\mathrm{i}\star}_{\alpha\beta} = \tfrac{1}{\omega_0}\tfrac{\mathrm{d}}{\mathrm{d}t}\gamma^{\mathrm{v}}_{\alpha\beta} + i^{\mathrm{g}}_{\alpha\beta} + k^{\mathrm{v}}_{\mathrm{p}}(e^{\star}_{\alpha\beta} - e_{\alpha\beta}), \tag{4b}$$

where $k^{\mathrm{v}}_{\mathrm{p}}$ denotes the proportional gain in the controller.

VI-Lim. When leveraging the VI-Lim, the dynamics of the voltage controller are given by

$$\tfrac{1}{\omega_0^2}\tfrac{\mathrm{d}^2}{\mathrm{d}t^2}\gamma^{\mathrm{v}}_{\alpha\beta} = k^{\mathrm{v}}_{\mathrm{r}}(e^{\star}_{\alpha\beta} - e_{\alpha\beta} - \psi(L_{\mathrm{vi}}\tfrac{\mathrm{d}}{\mathrm{d}t}i^{\mathrm{i}}_{\alpha\beta} + R_{\mathrm{vi}}i^{\mathrm{i}}_{\alpha\beta})) - \gamma^{\mathrm{v}}_{\alpha\beta}, \tag{5a}$$

where L_{vi} and R_{vi} are the virtual-impedance's inductance and resistance, respectively, and ψ is a threshold function that gradually enables the virtual impedance, as a function of the output current, once the current reaches the threshold, I_{th}. Using a threshold function to enable the VI is common practice for VI-current limiting concepts, though the particular implementation may differ. In this work, we define the threshold function as follows: [3]

$$\psi = \max\left(0, \tfrac{\|I^{\mathrm{i}\star}_{\mathrm{abc}}\|_\infty - I_{\mathrm{th}}}{I_{\max} - I_{\mathrm{th}}}\right). \tag{5b}$$

The reference for the current controller, $i^{\mathrm{i}\star}_{\alpha\beta}$, is determined by the voltage controller as

$$i^{\mathrm{i}\star}_{\alpha\beta} = \tfrac{1}{\omega_0}\tfrac{\mathrm{d}}{\mathrm{d}t}\gamma^{\mathrm{v}}_{\alpha\beta} + i^{\mathrm{g}}_{\alpha\beta} + k^{\mathrm{v}}_{\mathrm{p}}(e^{\star}_{\alpha\beta} - e_{\alpha\beta} + \psi(L_{\mathrm{vi}}\tfrac{\mathrm{d}}{\mathrm{d}t}i^{\mathrm{i}}_{\alpha\beta} + R_{\mathrm{vi}}i^{\mathrm{i}}_{\alpha\beta})). \tag{5c}$$

2.4. Primary Control

In this work, we restrict ourselves to a droop primary controller; however, all the analysis presented in this work can be repeated with another primary controller such as a virtual synchronous machine or virtual oscillator controller. The droop controller dynamics are captured by

$$\tfrac{\mathrm{d}}{\mathrm{d}t}\theta = \omega_0 + m_{\mathrm{p}}(P^{\star} - P), \tag{6a}$$

$$E^{\star} = E_0 + m_{\mathrm{q}}(Q^{\star} - Q), \tag{6b}$$

where θ denotes the reference angle of the GFM controls; ω_0 denotes the base frequency; m_{p} and m_{q} denote the $P-f$ and $Q-V$ droop gains, respectively; $E^{\star}$ denotes the reference voltage magnitude with E_0 being the base value; P and Q denote the positive sequence components of the output active and reactive power. Positive-sequence voltage and current signals are obtained by employing Park's transformation and filtering out the double line frequency ripple; $P^{\star}$ and $Q^{\star}$ denote the active and reactive output power set points. Note that the reference signal feeding the voltage controller, $e^{\star}_{\alpha\beta}$ (see (4a) and (5a)), is defined as

$$e^{\star}_{\alpha\beta} = \Gamma(\theta)[E^{\star}, 0]^{\top}.$$

3. Steady-state Equivalent Circuit

The equivalent circuit in steady state is represented in a direct-quadrature reference frame for positive- and negative-sequence domains. We next provide the derivation of this circuit focusing on one sub-system at a time. The level of detail is intentionally tapered off given space constraints.

3.1. Output LCL Filter

Consider the originating differential equations for the current in the grid-side inductance:

$$L_{\mathrm{g}}\tfrac{\mathrm{d}}{\mathrm{d}t}i^{\mathrm{g}}_{\mathrm{abc}} = e_{\mathrm{abc}} - v_{\mathrm{abc}} - R_{\mathrm{g}}i^{\mathrm{g}}_{\mathrm{abc}}. \tag{7}$$

Next, we will decompose each signal into positive- and negative-sequence components, and thereby rewrite (7) as:[1]

$$L_{\mathrm{g}}\tfrac{\mathrm{d}}{\mathrm{d}t}(i^{\mathrm{g}+}_{\mathrm{abc}} + i^{\mathrm{g}-}_{\mathrm{abc}}) = e^{+}_{\mathrm{abc}} + e^{-}_{\mathrm{abc}} - (v^{+}_{\mathrm{abc}} + v^{-}_{\mathrm{abc}}) - R_{\mathrm{g}}(i^{\mathrm{g}+}_{\mathrm{abc}} + i^{\mathrm{g}-}_{\mathrm{abc}}). \tag{8}$$

We next separate the dynamics into positive- and negative-sequence components:

$$\begin{aligned} L_{\mathrm{g}}\tfrac{\mathrm{d}}{\mathrm{d}t}(i^{\mathrm{g}+}_{\mathrm{abc}}) &= e^{+}_{\mathrm{abc}} - v^{+}_{\mathrm{abc}} - R_{\mathrm{g}}i^{\mathrm{g}+}_{\mathrm{abc}}, \\ L_{\mathrm{g}}\tfrac{\mathrm{d}}{\mathrm{d}t}(i^{\mathrm{g}-}_{\mathrm{abc}}) &= e^{-}_{\mathrm{abc}} - v^{-}_{\mathrm{abc}} - R_{\mathrm{g}}i^{\mathrm{g}-}_{\mathrm{abc}}. \end{aligned} \tag{9}$$

Balanced three-phase signals can be represented as rotating complex-valued dynamic phasors with positive-sequence signals rotating counter-clockwise and negative-sequence signals rotating clockwise. Rewriting the differential equations above in a form that invokes dynamic phasors of the involved variables yields:

$$L_{\mathrm{g}}\tfrac{\mathrm{d}}{\mathrm{d}t}(\underline{I}^{\mathrm{g}+}\mathrm{e}^{\jmath\omega t}) = \underline{E}^{+}\mathrm{e}^{\jmath\omega t} - \underline{V}^{+}\mathrm{e}^{\jmath\omega t} - R_{\mathrm{g}}\underline{I}^{\mathrm{g}+}\mathrm{e}^{\jmath\omega t},$$

$$L_{\mathrm{g}}\tfrac{\mathrm{d}}{\mathrm{d}t}(\underline{I}^{\mathrm{g}-}\mathrm{e}^{-\jmath\omega t}) = \underline{E}^{-}\mathrm{e}^{-\jmath\omega t} - \underline{V}^{-}\mathrm{e}^{-\jmath\omega t} - R_{\mathrm{g}}\underline{I}^{\mathrm{g}-}\mathrm{e}^{-\jmath\omega t}.$$

[1] In this work, we do not consider zero-sequence signals because of the absence of a neutral line in the GFM architecture in Fig. 1. To derive the model for a three-phase four-wire inverter, zero sequence components must be added to the analysis.

Simplifying the derivative terms above and applying elementary algebraic manipulations yields

$$L_{\mathrm{g}}(\tfrac{\mathrm{d}}{\mathrm{d}t}\underline{I}^{\mathrm{g}+} + \jmath\omega I^{\mathrm{g}+}) = \underline{E}^{+} - \underline{V}^{+} - R_{\mathrm{g}}\underline{I}^{\mathrm{g}+},$$
$$L_{\mathrm{g}}(\tfrac{\mathrm{d}}{\mathrm{d}t}\underline{I}^{\mathrm{g}-} - \jmath\omega I^{\mathrm{g}-}) = \underline{E}^{-} - \underline{V}^{-} - R_{\mathrm{g}}\underline{I}^{\mathrm{g}-}.$$

We can project complex-valued phasors onto a dq-frame, with the d-axis representing the real axis, and the q-axis, the imaginary one (without loss of generality). Further, the imaginary unit, $\jmath$, denotes a $+90^{\circ}$ rotation in the dq-plane. Notice that, for the negative-sequence plane, $\jmath$ means a -90° rotation in the dq-plane. With these considerations, we have

$$L_{\mathrm{g}}(\tfrac{\mathrm{d}}{\mathrm{d}t}I_{\mathrm{dq}}^{\mathrm{g}+} + \omega\Gamma(\tfrac{\pi}{2})I_{\mathrm{dq}}^{\mathrm{g}+}) = E_{\mathrm{dq}}^{+} - V_{\mathrm{dq}}^{+} - R_{\mathrm{g}}I_{\mathrm{dq}}^{\mathrm{g}+},$$
$$L_{\mathrm{g}}(\tfrac{\mathrm{d}}{\mathrm{d}t}I_{\mathrm{dq}}^{\mathrm{g}-} + \omega\Gamma(\tfrac{\pi}{2})I_{\mathrm{dq}}^{\mathrm{g}-}) = E_{\mathrm{dq}}^{-} - V_{\mathrm{dq}}^{-} - R_{\mathrm{g}}I_{\mathrm{dq}}^{\mathrm{g}-}.$$

As soon as we transfer to a direct-quadrature frame, we need to define a reference to which we relate the dq components. All the control signals are defined in the local dq frame, for which the primary-controller angle, θ is the zero reference. The grid-side physical signals are defined in the global DQ frame, for which the grid voltage, V_{g}, is the zero reference. For convenience, we transform all signals into the local dq frame, for which we define $V_{\mathrm{dq}}^{\pm} = \Gamma(-\delta)[V_{\mathrm{DQ}}^{\pm},\, 0]^{\top}$, where δ denotes the angle difference between the local and global frame, and $E_{\mathrm{dq}}^{\star\pm} = [E^{\star\pm},\, 0]^{\top}$. Since we are interested in capturing steady-state operation, we move on to setting derivatives to zero:

$$0 = E_{\mathrm{dq}}^{\pm} - V_{\mathrm{dq}}^{\pm} - L_{\mathrm{g}}\omega\Gamma(\tfrac{\pi}{2})I_{\mathrm{dq}}^{\mathrm{g}\pm} - R_{\mathrm{g}}I_{\mathrm{dq}}^{\mathrm{g}\pm}. \tag{10}$$

In a similar fashion, we can derive the following equations for the filter capacitor:

$$0 = I_{\mathrm{dq}}^{\mathrm{i}\pm} - I_{\mathrm{dq}}^{\mathrm{g}\pm} - \omega C\Gamma(\tfrac{\pi}{2})E_{\mathrm{dq}}^{\pm}, \tag{11}$$

and the following ones for the inverter-side inductive filter:

$$0 = U_{\mathrm{dq}}^{\pm} - E_{\mathrm{dq}}^{\pm} - L_{\mathrm{i}}\omega\Gamma(\tfrac{\pi}{2})I_{\mathrm{dq}}^{\mathrm{i}\pm} - R_{\mathrm{i}}I_{\mathrm{dq}}^{\mathrm{i}\pm}. \tag{12}$$

3.2. Current Controller

SatLim. Consider the dynamics for the current controller with saturation limiting in (2). We can follow along the same process as the dynamics of the grid-side inductance in Section 3.1 to recover the following algebraic equations that describe steady-state operation:

$$\begin{aligned} -\tfrac{\omega^2}{\omega_0^2}\gamma_{\mathrm{dq}}^{\mathrm{c}\pm} &= k_{\mathrm{r}}^{\mathrm{c}}(\rho I_{\mathrm{dq}}^{\mathrm{i}\star\pm} - I_{\mathrm{dq}}^{\mathrm{i}\pm}) - \gamma_{\mathrm{dq}}^{\mathrm{c}\pm}, \\ \tfrac{\omega}{\omega_0}\Gamma(\tfrac{\pi}{2})\gamma_{\mathrm{dq}}^{\mathrm{c}\pm} &= U_{\mathrm{dq}}^{\pm} - E_{\mathrm{dq}}^{\pm} - k_{\mathrm{p}}^{\mathrm{c}}(\rho I_{\mathrm{dq}}^{\mathrm{i}\star\pm} - I_{\mathrm{dq}}^{\mathrm{i}\pm}). \end{aligned} \tag{13}$$

VI-Lim. In the case of the current controller implemented with virtual impedance imiting (3), we get the following algebraic equations in steady state:

$$\begin{aligned} -\tfrac{\omega^2}{\omega_0^2}\gamma_{\mathrm{dq}}^{\mathrm{c}\pm} &= k_{\mathrm{r}}^{\mathrm{c}}(I_{\mathrm{dq}}^{\mathrm{i}\star\pm} - I_{\mathrm{dq}}^{\mathrm{i}\pm}) - \gamma_{\mathrm{dq}}^{\mathrm{c}\pm}, \\ \tfrac{\omega}{\omega_0}\Gamma(\tfrac{\pi}{2})\gamma_{\mathrm{dq}}^{\mathrm{c}\pm} &= U_{\mathrm{dq}}^{\pm} - E_{\mathrm{dq}}^{\pm} - k_{\mathrm{p}}^{\mathrm{c}}(I_{\mathrm{dq}}^{\mathrm{i}\star\pm} - I_{\mathrm{dq}}^{\mathrm{i}\pm}). \end{aligned} \tag{14}$$

3.3. Voltage Controller

SatLim. Next, we consider the dynamics for the voltage controller with saturation limiting in (4). We can follow along the same process as the dynamics of the grid-side inductance outlined in Section 3.1 to recover the following algebraic equations that describe steady-state operation:

$$\tfrac{\omega}{\omega_0}\Gamma(\tfrac{\pi}{2})\gamma_{\mathrm{dq}}^{\mathrm{v}\pm} = I_{\mathrm{dq}}^{\mathrm{i}\star\pm} - I_{\mathrm{dq}}^{\mathrm{g}\pm} - k_{\mathrm{p}}^{\mathrm{v}}(E_{\mathrm{dq}}^{\star\pm} - E_{\mathrm{dq}}^{\pm}), \tag{15}$$
$$-\tfrac{\omega^2}{\omega_0^2}\gamma_{\mathrm{dq}}^{\mathrm{v}\pm} = k_{\mathrm{r}}^{\mathrm{v}}(E_{\mathrm{dq}}^{\star\pm} - E_{\mathrm{dq}}^{\pm} - k_{\mathrm{w}}(1-\rho)I_{\mathrm{dq}}^{\mathrm{i}\star\pm}) - \gamma_{\mathrm{dq}}^{\mathrm{v}\pm}.$$

VI-Lim. In the case of the voltage controller implemented with virtual impedance limiting (5), we get the following algebraic equations in steady state:

$$\begin{aligned} \tfrac{\omega}{\omega_0}\Gamma(\tfrac{\pi}{2})\gamma_{\mathrm{dq}}^{\mathrm{v}\pm} &= I_{\mathrm{dq}}^{\mathrm{i}\star\pm} - I_{\mathrm{dq}}^{\mathrm{g}\pm} - k_{\mathrm{p}}^{\mathrm{v}}(E_{\mathrm{dq}}^{\star\pm} - E_{\mathrm{dq}}^{\pm} \\ &\quad - \psi(L_{\mathrm{vi}}\omega\Gamma(\tfrac{\pi}{2})I_{\mathrm{dq}}^{\mathrm{i}\pm} + R_{\mathrm{vi}}I_{\mathrm{dq}}^{\mathrm{i}\pm})), \\ -\tfrac{\omega^2}{\omega_0^2}\gamma_{\mathrm{dq}}^{\mathrm{v}\pm} &= -\gamma_{\mathrm{dq}}^{\mathrm{v}\pm} + k_{\mathrm{r}}^{\mathrm{v}}(E_{\mathrm{dq}}^{\star\pm} - E_{\mathrm{dq}}^{\pm} \\ &\quad - \psi(L_{\mathrm{vi}}\omega\Gamma(\tfrac{\pi}{2})I_{\mathrm{dq}}^{\mathrm{i}\pm} + R_{\mathrm{vi}}I_{\mathrm{dq}}^{\mathrm{i}\pm})). \end{aligned} \tag{16}$$

3.4. Synthesizing an Equivalent Circuit

We recognize that during steady-state $\omega \approx \omega_0$. Applying this approximation to (13) and (15) yields:

$$\begin{aligned} 0 &= \rho I_{\mathrm{dq}}^{\mathrm{i}\star\pm} - I_{\mathrm{dq}}^{\mathrm{i}\pm}, \\ 0 &= E_{\mathrm{dq}}^{\star\pm} - E_{\mathrm{dq}}^{\pm} - k_{\mathrm{w}}(1-\rho)I_{\mathrm{dq}}^{\mathrm{i}\star\pm}. \end{aligned} \tag{17}$$

Similarly, applying it to (14) and (16) results in

$$\begin{aligned} 0 &= I_{\mathrm{dq}}^{\mathrm{i}\star\pm} - I_{\mathrm{dq}}^{\mathrm{i}\pm}, \\ 0 &= E_{\mathrm{dq}}^{\star\pm} - E_{\mathrm{dq}}^{\pm} - \psi(L_{\mathrm{vi}}\omega\Gamma(\tfrac{\pi}{2})I_{\mathrm{dq}}^{\mathrm{i}\pm} + R_{\mathrm{vi}}I_{\mathrm{dq}}^{\mathrm{i}\pm}). \end{aligned} \tag{18}$$

SatLim. Let us now focus on the derivation of an equivalent-circuit model for the architecture with saturation limiting. We can construct the following three equations by manipulating (10), (11), and (17):

$$E_{\mathrm{dq}}^{\star\pm} = E_{\mathrm{dq}}^{\pm} + \rho I_{\mathrm{dq}}^{\mathrm{i}\star\pm} \cdot \tfrac{k_{\mathrm{w}}(1-\rho)}{\rho}, \tag{19a}$$

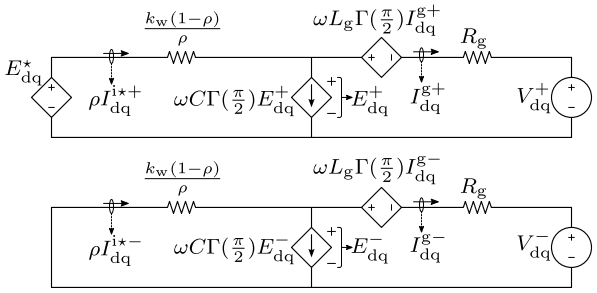

Figure 2. Positive- and negative-sequence steady-state equivalent-circuit models with saturation limiting.

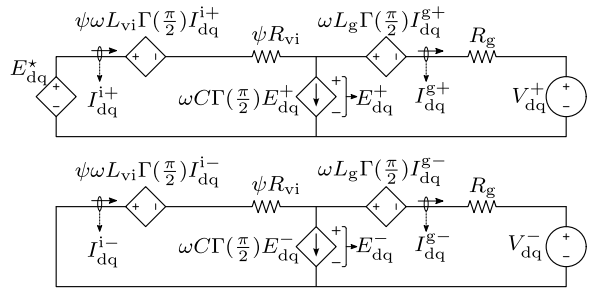

Figure 3. Positive- and negative-sequence steady-state equivalent-circuit models with virtual impedance limiting.

$$E^{\pm}_{\mathrm{dq}} = V^{\pm}_{\mathrm{dq}} + L_{\mathrm{g}}\omega\Gamma(\tfrac{\pi}{2})I^{\mathrm{g}\pm}_{\mathrm{dq}} + R_{\mathrm{g}}I^{\mathrm{g}\pm}_{\mathrm{dq}}, \tag{19b}$$

$$\omega C\Gamma(\tfrac{\pi}{2})E^{\pm}_{\mathrm{dq}} = \rho I^{\mathrm{i}\star\pm}_{\mathrm{dq}} - I^{\mathrm{g}\pm}_{\mathrm{dq}}. \tag{19c}$$

We can map (19) to the equivalent circuits in Fig. 2, with (19a) and (19b) capturing the KVL equations around the two loops and (19c) capturing KCL at the node with voltage $E^{\pm}_{\mathrm{dq}}$. Notice that the driving voltage in the negative-sequence equivalent circuit, $E^{\star-}_{\mathrm{dq}} = 0$ because the primary controller is operating only in the positive sequence, i.e., the output-power feedback to the primary controller is relayed to positive sequence only.

VI-Lim. Next, we focus on the derivation of an equivalent-circuit model for the architecture with virtual-impedance limiting. We can construct the following three equations by manipulating (10), (11), and (18):

$$E^{\star\pm}_{\mathrm{dq}} = E^{\pm}_{\mathrm{dq}} + \psi L_{\mathrm{vi}}\omega\Gamma(\tfrac{\pi}{2})I^{\mathrm{i}\pm}_{\mathrm{dq}} + I^{\mathrm{i}\pm}_{\mathrm{dq}}\cdot\psi R_{\mathrm{vi}}, \tag{20a}$$

$$E^{\pm}_{\mathrm{dq}} = V^{\pm}_{\mathrm{dq}} + L_{\mathrm{g}}\omega\Gamma(\tfrac{\pi}{2})I^{\mathrm{g}\pm}_{\mathrm{dq}} + R_{\mathrm{g}}I^{\mathrm{g}\pm}_{\mathrm{dq}}, \tag{20b}$$

$$\omega C\Gamma(\tfrac{\pi}{2})E^{\pm}_{\mathrm{dq}} = I^{\mathrm{i}\pm}_{\mathrm{dq}} - I^{\mathrm{g}\pm}_{\mathrm{dq}}. \tag{20c}$$

We can map (20) to the equivalent circuits in Fig. 3, with (20a) and (20b) capturing the KVL equations around the two loops and (20c) capturing KCL at the node with voltage $E^{\pm}_{\mathrm{dq}}$. As was the case with the saturation limiting, the driving voltage in the negative-sequence equivalent circuit, $E^{\star-}_{\mathrm{dq}} = 0$.

Notice from (2b) and (5b) that ρ and ψ are piecewise continuous functions. This aspect can challenge implementation. To counter the computational complexity, we adopt the following continuous approximations

$$\rho' = -\tfrac{1}{2}\Big(-1-\tfrac{I_{\max}}{\|I^{\mathrm{i}\star}_{\mathrm{abc}}\|_\infty}+\sqrt{\Big(\tfrac{I_{\max}}{\|I^{\mathrm{i}\star}_{\mathrm{abc}}\|_\infty}-1\Big)^2}\Big), \tag{21}$$

$$\psi' = \tfrac{1}{2}\Big(\tfrac{\|I^{\mathrm{i}\star}_{\mathrm{abc}}\|_\infty - I_{\mathrm{th}}}{I_{\max}-I_{\mathrm{th}}}+\sqrt{\Big(\tfrac{\|I^{\mathrm{i}\star}_{\mathrm{abc}}\|_\infty - I_{\mathrm{th}}}{I_{\max}-I_{\mathrm{th}}}\Big)^2}\Big). \tag{22}$$

Similarly, $\|I^{\mathrm{i}\star}_{\mathrm{abc}}\|_\infty$ in the expressions for ρ' and ψ' is approximated with a continuous function. In particular, instead of computing

$$\|I^{\mathrm{i}\star}_{\mathrm{abc}}\|_\infty = \max(|I^{\mathrm{i}\star}_{\mathrm{a}}|,\, |I^{\mathrm{i}\star}_{\mathrm{b}}|,\, |I^{\mathrm{i}\star}_{\mathrm{c}}|),$$

we adopt the following p-norm approximation (with sufficiently high p):

$$\|I^{\mathrm{i}\star}_{\mathrm{abc}}\|_\infty \approx \left(|I^{\mathrm{i}\star}_{\mathrm{a}}|^p + |I^{\mathrm{i}\star}_{\mathrm{b}}|^p + |I^{\mathrm{i}\star}_{\mathrm{c}}|^p\right)^{\frac{1}{p}}. \tag{23}$$

The magnitudes of the phase-current references, $|I^{\mathrm{i}\star}_{n}|$, can be computed via the theory of symmetrical components and Fortescue's transformation:

$$\begin{aligned}
|I^{\mathrm{i}\star}_{\mathrm{a}}| &= |I^{\mathrm{i}\star+}_{\mathrm{dq}} + I^{\mathrm{i}\star-}_{\mathrm{dq}}|,\\
|I^{\mathrm{i}\star}_{\mathrm{b}}| &= |\Gamma(\tfrac{4\pi}{3})I^{\mathrm{i}\star+}_{\mathrm{dq}} + \Gamma(\tfrac{2\pi}{3})I^{\mathrm{i}\star-}_{\mathrm{dq}}|,\\
|I^{\mathrm{i}\star}_{\mathrm{c}}| &= |\Gamma(\tfrac{2\pi}{3})I^{\mathrm{i}\star+}_{\mathrm{dq}} + \Gamma(\tfrac{4\pi}{3})I^{\mathrm{i}\star-}_{\mathrm{dq}}|.
\end{aligned} \tag{24}$$

To solve the system of nonlinear algebraic equations, we combine the equations (6a), (6b), (19), (21), (23), and (24) for SatLim, or (6a), (6b), (20), (22), (23), and (24) for VI-Lim, into a system of 19 equations with 19 unknowns. Under balanced conditions, the equivalent-circuit models to be leveraged for steady-state analysis are the same as the positive-sequence circuits in Fig. 2 and 3.

4. Simulation Results

In this section, we put our steady-state equivalent-circuit GFM models to the test by comparing their outputs with time-domain trajectories resulting from full-order EMT simulations set up in MATLAB-Simulink. We emulate faults —both unbalanced and balanced—at the LCL-filter terminals while leveraging either the SatLim or VI-Lim in the

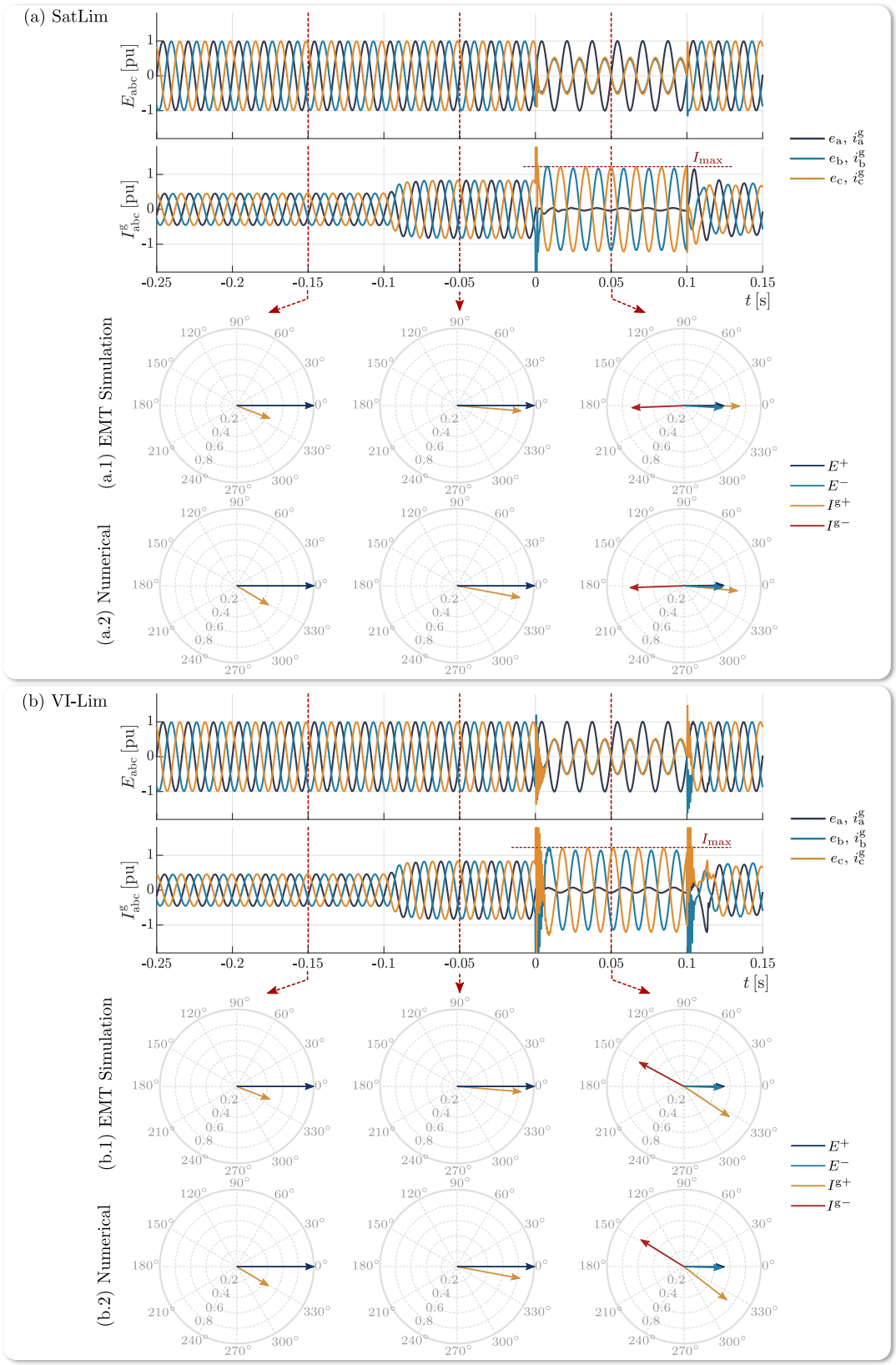

Figure 4. Comparative results for the unbalanced fault scenario between (a.1) the EMT simulations and (a.2) the numerically computed phasors from the equivalent-circuit models.

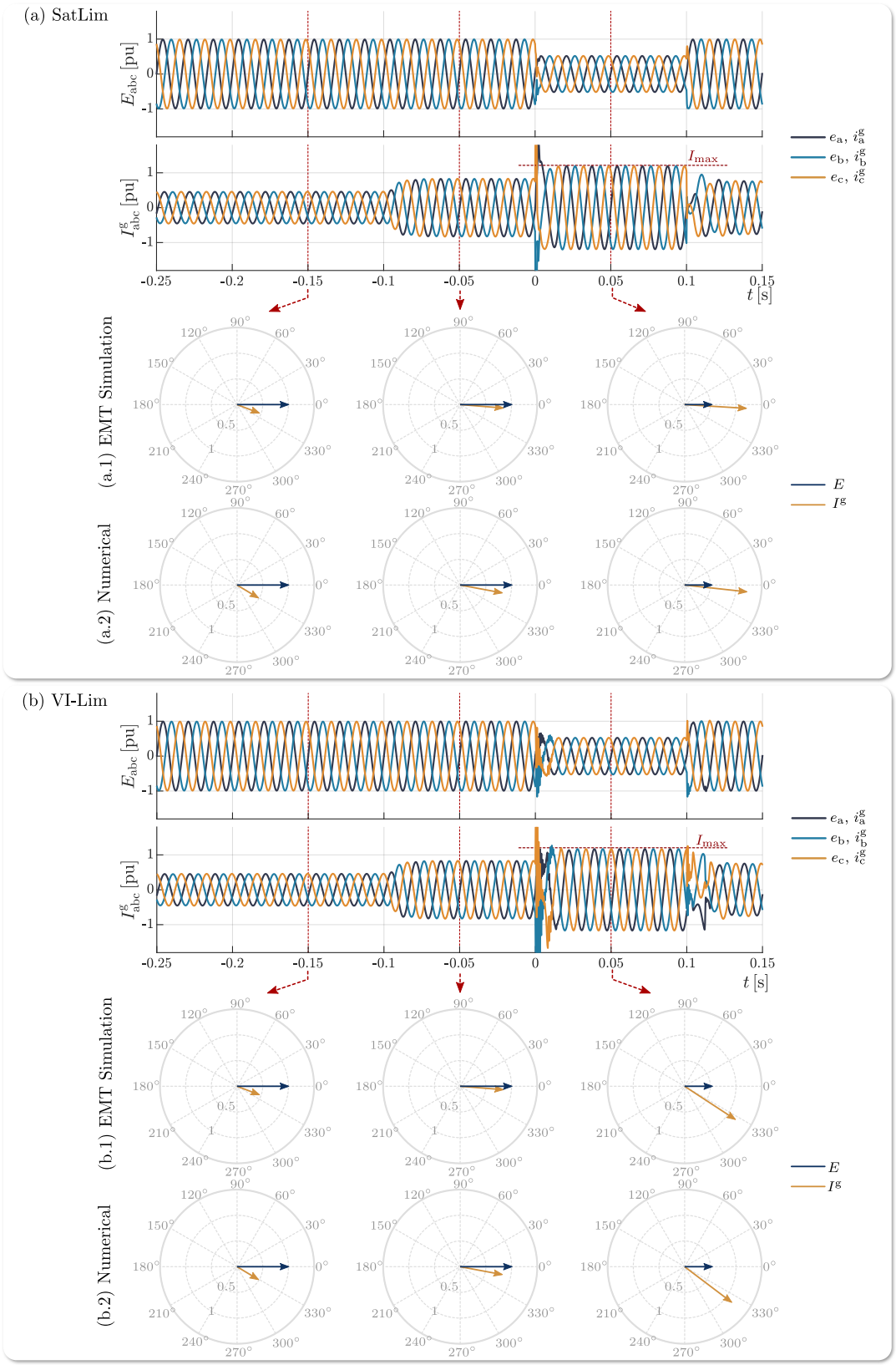

Figure 5. Comparative results for the balanced fault scenario between (b.1) the EMT simulations and (b.2) the numerically computed phasors from the equivalent-circuit models.

Table 1. Nominal Inverter Parameters & Inputs.

Parameter	Value	Unit	Parameter	Value	Unit
ω_0	$2\pi 60$	$\frac{\text{rad}}{\text{s}}$	k_{p}^{c}	0.9800	pu
$\omega_0 L_{\text{i}}$	0.0196	pu	k_{r}^{c}	0.695	pu
R_{i}	0.0139	pu	k_{p}^{v}	1.4480	pu
$\omega_0 C$	0.1086	pu	k_{r}^{v}	5.1484	pu
$\omega_0 L_{\text{g}}$	0.0294	pu	m_{p}	1	%
R_{g}	0.0209	pu	m_{q}	4	%
$I_{\max}$	1.2	pu	k_{w}	$(k_{\text{p}}^{\text{v}})^{-1}$	pu
$\omega_0 L_{\text{vi}}$	0.5357	pu	I_{th}	1	pu
R_{vi}	0.6384	pu			

inverter controls. For the unbalanced fault, we apply a 0.5-pu voltage drop/rise in the positive/negative sequence grid voltage. This is a typical fault characteristic of a severe line-to-line fault. For the balanced fault, we apply a positive sequence voltage drop to the grid voltage. We compute the steady-state output voltage and current of the inverter pre-fault and during the fault, and compare that with the steady-state values obtained from the EMT simulation. Complex steady-state voltage and current phasors are extracted from the EMT simulation using discrete Fourier transformations and separated into sequence components by leveraging symmetrical components theory. This process inherently creates some numerical error in the signal processing stage, which translates into a small mismatch between the EMT and numerically obtained complex phasors (see results in Fig. 4 and Fig. 5). For the EMT simulation, we use the GFM control architecture in Fig. 1. The inverter parameters are listed in Table 1.

Figure 4 collectively shows the results for the unbalanced fault while using either (a) the SatLim or (b) the VI-Lim in the inverter controls. The time-domain signals illustrate the LCL capacitor voltage, and the grid-side LCL current for the EMT simulation. At $t = -0.1\,\text{s}$, we apply a step change in the power set point from $P^\star = 0.4\,\text{pu}$ to $P^\star = 0.8\,\text{pu}$, which is noticeable by the increase in output current. At $t = 0\,\text{s}$, we apply the unbalanced fault for a duration of $100\,\text{ms}$. Notice that the phase currents are scaled by the limiter such that the highest phase current does not surpass the limit of $1.2\,\text{pu}$. For the pre-fault period where $P^\star = 0.4\,\text{pu}$ and $P^\star = 0.8\,\text{pu}$, and during the fault, we compare the steady-state attributes from the numerical computation with the EMT simulation. We display the results in the form of sequence voltage and current phasors, as shown in Fig. 4(a.1), (b.1) for the EMT simulations and Fig. 4(a.2), (b.2) for the numerical computation leveraging the GFM equivalent-circuit models. We observe a close match between the EMT simulation and the equivalent-circuit models, both during pre-fault balanced conditions, as well as during the unbalanced fault. Further, notice that the pre-fault phasor plots are identical for SatLim and VI-Lim because the limiter is not engaging during normal operation; however, a different behavior during fault conditions is noticeable due to the actions of the limiter. The SatLim behaves as a resistance while the virtual impedance has an impedance angle set to $40°$.

To illustrate that the same equivalent GFM network models can be leveraged for balanced faults, we present balanced-fault results in Fig. 5.

5. Conclusions & Future Work

This paper presented a methodology to derive steady-state GFM equivalent-circuit models under unbalanced steady-state operating conditions. The model derivation is outlined starting with the dynamic state equations of a stationary-frame controlled GFM inverter. The models include two well-known current-limiting concepts; the current-reference saturation and virtual impedance limiter, and are extendable to other GFM control architectures. We validate the models against full-order EMT simulations and illustrate a tight match. Steady-state GFM models hold much value in, e.g., power system protection studies and design, large-signal stability analysis, or power flow analyses, in power grids with a mix of IBRs. We intend to pursue these applications as future work.

Acknowledgements

This work was authored in part by the National Renewable Energy Laboratory, operated by Alliance for Sustainable Energy, LLC, for the U.S. Department of Energy (DOE) under Contract No. DE-AC36-08GO28308. This work was supported by the Laboratory Directed Research and Development (LDRD) Program at NREL and the U.S. Department of Energy Office of Energy Efficiency and Renewable Energy under the Solar Energy Technologies Office Award Number 38637. This research was also supported by the Grid Modernization Initiative of DOE as part of its Grid Modernization Laboratory Consortium, a strategic partnership between DOE and the national laboratories to bring together leading experts, technologies, and resources to collaborate on the goal of modernizing the nation's grid. The views expressed in the article do not necessarily represent the views of the DOE or the U.S. Government. The U.S.

References

[1] Y. Lin, J. H. Eto, B. B. Johnson, J. D. Flicker, R. H. Lasseter, H. N. Villegas Pico, G.-S. Seo, B. J. Pierre, and A. Ellis, "Research roadmap on grid-forming inverters," National Renewable Energy Lab, Tech. Rep., 2020.

[2] D. Venkatramanan, R. Henriquez-Auba, M. R. K. Rachi, J. T. Bui, M. K. Singh, D. Ramasubramanian, A. Hoke, B. Kroposki, and S. Dhople, "Grid-forming Inverter Technology Specifications: A Review of Research Reports & Roadmaps," UNIFI Technical Report, UNIFI-2022-1-1, Tech. Rep., November 2022.

[3] N. Baeckeland, D. Venkatramanan, M. Kleemann, and S. Dhople, "Stationary-frame grid-forming inverter control architectures for unbalanced fault-current limiting," *IEEE Trans. Energy Convers.*, vol. 37, no. 4, pp. 2813–2825, 2022.

[4] R. Rosso, S. Engelken, and M. Liserre, "On the implementation of an frt strategy for grid-forming converters under symmetrical and asymmetrical grid faults," *IEEE Trans. Ind. Appl.*, vol. 57, no. 5, pp. 4385–4397, 2021.

[5] P. Bhagwat and D. Groß, "Three-phase grid-forming droop control for unbalanced systems and fault ride through," in *IEEE Power & Energy Society General Meeting*, 2023.

[6] B. Fan and X. Wang, "Equivalent circuit model of grid-forming converters with circular current limiter for transient stability analysis," *IEEE Trans. Power Syst.*, vol. 37, no. 4, pp. 3141–3144, 2022.

[7] A. D. Paquette and D. M. Divan, "Virtual impedance current limiting for inverters in microgrids with synchronous generators," *IEEE Trans. Ind. Appl.*, vol. 51, no. 2, pp. 1630–1638, 2015.

[8] M. Shirazi, D. Groß, D. Light, J. VanderMeer, and T. Morgan, "Evaluation of current-limiting strategies for grid-forming inverters," in *IEEE Energy Conversion Congress and Exposition*, 2023, pp. 1067–1074.

[9] J. Freytes, J. Li, G. de Préville, and M. Thouvenin, "Grid-forming control with current limitation for MMC under unbalanced fault ride-through," *IEEE Trans. Power Del.*, vol. 36, no. 3, pp. 1914–1916, 2021.

[10] S. S. Nudehi and D. Groß, "Grid-forming control of three-phase and single-phase converters across unbalanced transmission and distribution systems," *IEEE Trans. Power Syst.*, vol. 38, no. 6, pp. 5687–5700, 2023.

[11] T. Kim, N. G. Barry, W. Kim, S. Santoso, W. Wang, R. C. Dugan, and D. Ramasubramanian, "Voltage balancing capability of grid-forming inverters," *IEEE Open Access Journal of Power and Energy*, vol. 9, pp. 479–488, 2022.

[12] D. Chatterjee, N. G. Barry, T. Kim, W. Kim, and S. Santoso, "Voltage balancing of grid-forming inverters in unbalanced, islanded microgrids," in *IEEE Power & Energy Society General Meeting*, 2023.

[13] M. Awal, M. R. K. Rachi, H. Yu, I. Husain, and S. Lukic, "Double synchronous unified virtual oscillator control for asymmetrical fault ride-through in grid-forming voltage source converters," *IEEE Trans. Power Del.*, vol. 38, no. 6, pp. 6759–6763, 2023.

[14] M. A. Desai, X. He, L. Huang, and F. Dörfler, "Saturation-informed current-limiting control for grid-forming converters," 2024, arXiv:2404.07682.

[15] H. Wu, X. Wang, and L. Zhao, "Design considerations of current-limiting control for grid-forming capability enhancement of vscs under large grid disturbances," *IEEE Trans. Power Electron.*, 2024.

[16] S. Seo, E. Muljadi, Q. Nguyen, S. Datta, N. A. Samaan, B. Vyakaranam, W. Du, Y. Liu, Y. Chen, J. Kim, and M. Maharjan, "Modified steady-state power flow for grid with high penetration of inverter-based resource," in *IEEE Energy Conversion Congress and Exposition*, 2023, pp. 266–272.

[17] O. Ajala, T. Roberts, and A. Domínguez-García, "Power-flow formulation for inverter-based grids," in *IEEE Power & Energy Society General Meeting*, 2023.

[18] N. Turner-Bandele, A. Pandey, and L. Pileggi, "Analytical inverter-based distributed generator model for power flow analysis," in *IEEE Power & Energy Society General Meeting*, 2021.

[19] D. Li, Y. Su, F. Wang, M. Olama, B. Ollis, and M. Ferrari, "Power flow models of grid-forming inverters in unbalanced distribution grids," *IEEE Trans. Power Syst.*, vol. 39, no. 2, pp. 4311–4322, 2024.

[20] B. Mahamedi and J. E. Fletcher, "The equivalent models of grid-forming inverters in the sequence domain for the steady-state analysis of power systems," *IEEE Trans. Power Syst.*, vol. 35, no. 4, pp. 2876–2887, 2020.

[21] W. Du, Y. Liu, R. Huang, F. K. Tuffner, J. Xie, and Z. Huang, "Positive-sequence phasor modeling of droop-controlled, grid-forming inverters with fault current limiting function," in *IEEE Power and Energy Society Innovative Smart Grid Technologies Conference*, 2022.

[22] V. C. Cunha, T. Kim, N. Barry, P. Siratarnsophon, S. Santoso, W. Freitas, D. Ramasubramanian, and R. C. Dugan, "Generalized formulation of steady-state equivalent circuit models of grid-forming inverters," *IEEE Open Access Journal of Power and Energy*, vol. 8, pp. 352–364, 2021.

[23] T. Kim, N. G. Barry, W. Kim, S. Santoso, V. C. Cunha, W. Freitas, W. Wang, R. Dugan, D. Ramasubramanian, and A. Maitra, "Modeling and simulation of short-circuit faults in inverter-based microgrids using steady-state equivalent circuits," in *IEEE Power & Energy Society General Meeting*, 2022.

[24] A. Yazdani and R. Iravani, *Voltage-sourced converters in power systems: modeling, control, and applications*. John Wiley & Sons, 2010.

[25] D. Venkatramanan, M. K. Singh, O. Ajala, A. Domínguez-García, and S. Dhople, "Integrated system models for networks with generators & inverters," in *Proc. 11th Bulk Power Systems Dynamics and Control Symposium*, 2022. Available at: arXiv preprint arXiv:2203.08253.